ORIGINAL PAPER

Mechanisms of Block Instability at the Toe of a Slowly Deforming Rock Slope

Tommaso Carlà[1] · Giovanni Gigli[1] · Luca Lombardi[1] · Massimiliano Nocentini[2] · Teresa Gracchi[1] · Guglielmo Rossi[2] · Carlo Tacconi Stefanelli[1] · Federico Raspini[1] · Giandomenico Fubelli[3] · Nicola Casagli[1]

Abstract

Steep alpine rock slopes undergoing deformation may give rise to concurrent landslide hazards of different type and magnitude. The underlying mechanisms of instability are often challenging to investigate due to their inherent complexity; furthermore, they can occur on poorly accessible terrain, preventing the collection of data by means of traditional field techniques or even inhibiting awareness of hazards. This paper focuses upon one such case, in which a major transportation corridor running along the floor of the Aosta Valley (Western Italian Alps) is affected by significant—and until recently unknown—rockfall hazards promoted by a previously collapsed rockslide still deforming slowly at elevations almost 600 m above the road. In particular, two large discrete blocks (volume $> 10^3$ m^3) lie precariously at the toe of the slide and could fall downslope at extremely rapid velocity. The design of countermeasures for the stabilization or removal of these blocks would require the assessment of their mechanical interaction with the bedrock and degree of internal fracturing (i.e., possible pervasive damage within the blocks). We perform this task by first exploring potential kinematic styles and damage patterns at failure according to a series of preliminary finite-element models. We then use detailed displacement measurements from remote sensing and in situ monitoring, in conjunction with repeat topographic surveying from a terrestrial laser scanner (TLS) and a drone laser scanner (DLS), to reconstruct the actual kinematics of the blocks. The results substantiate the hypothesis that instability is primarily controlled by transient degradation of friction on a through-going basal rupture surface. Development of a large tensile fracture in one of the two blocks is inferred to be conditioned by increased non-planarity of the slipping joint in comparison with the other block. We highlight that optimized integration of cutting-edge rock slope investigation tools can help address otherwise unresolved key aspects of complex instabilities in steep mountainous areas.

Highlights

- Two large discrete blocks at the toe of a slowly deforming and highly disaggregated rock slope pose significant concerns to a major transportation corridor in the Western Italian Alps. Knowledge of the underlying mechanisms of instability is required to design mitigation measures, but traditional site characterization is impossible due to difficult terrain.
- Preliminary numerical modelling, slope monitoring, and repeat topographic surveying are integrated into a coordinated analysis framework to explore kinematic styles, damage patterns, and overall modes of failure.
- It is shown that the blocks are likely affected by transient degradation of friction on a through-going basal rupture surface of varying roughness, and translate towards the steep apex of the adjacent talus cone as mostly individual entities with negligible influence of brittle fracture damage.

✉ Tommaso Carlà
  tommaso.carla@unifi.it

[1] Department of Earth Sciences, Università Degli Studi di Firenze, Via Giorgio La Pira 4, 50121 Florence, Italy

[2] Center for Civil Protection, Università Degli Studi Di Firenze, Largo Enrico Fermi 2, 50125 Florence, Italy

[3] Department of Earth Sciences, Università di Torino, Via Valperga Caluso 35, 10125 Turin, Italy

1 Introduction

Large rock slope instabilities show a range of possible deformation behavior. They may move slowly for periods of thousands of years (Crosta et al. 2017), promote the episodic detachment of comparatively small blocks (Gschwind et al. 2019), eventually become inactive, or conversely fail catastrophically ("collapse") by experiencing sudden disaggregation and large displacement at the overall slope-scale (Glastonbury and Fell 2010). While predicting the most likely outcome is already a challenging task, deformation may persist even well after collapse because of residual imbalances of forces across the slope, modifications to slope kinematics arising from the reshaped topography, degradation of rock mass strength, and external triggers. This late activity tends to be of lower intensity and involve smaller volumes (Leroueil et al. 1996); however, associated risks can remain equally as high. If substantial parts of the slide mass do not vacate the source area upon collapse, discrete blocks may be left lying near limit equilibrium on steep slopes. Complete kinematic release may subsequently be induced by time-dependent and dynamic processes, giving rise to secondary rockfalls or rock avalanches.

Linear transportation corridors in narrow alpine valleys are frequently impacted by these kinds of landslide hazards. Contributing factors include the ruggedness of adjacent mountainous flanks; topographic restraints (i.e., lack of viable alternative routes); the enhanced rate of mass wasting processes during paraglacial readjustment (Riva et al. 2018; Spreafico et al. 2021); and the fact that many of these critical infrastructures were designed decades ago employing rudimentary principles of rock slope hazard assessment. As a result, corridor segments have, on occasion, been discovered to intersect the runout path of potentially destructive landslides that were mischaracterized or altogether overlooked prior to construction (Strouth and Eberhardt 2009). Adequate corridor safety may be restored by implementing early warning procedures, protection structures, or slope remedial works. To that aim, a prerequisite is to gain comprehensive knowledge about the underlying mechanisms of the newly detected hazard. Such an investigation benefits from an integrated approach, whereby coordinated use of multiple survey and modelling techniques compensates for the limitations inherent to exclusive use of a single technique (Stead et al. 2012). Notable examples, to name some, have been documented by Gigli et al. (2011), Brideau et al. (2011, 2012), Firpo et al. (2011), Gischig et al. (2011), Sturzenegger and Stead (2012), Francioni et al. (2014, 2015), Havaej et al. (2016), Paronuzzi et al. (2016), Spreafico et al. (2016), Carlà et al. (2021), Donati et al. (2021), and Rechberger and Zangerl (2022).

In the present work, we report on the investigation of a complex rockfall–rockslide hazard scenario near the town of Quincinetto, at the downstream end of the Aosta Valley in the Western Italian Alps. The slope presumably collapsed during a retreat phase of the former Dora Baltea Glacier, which dates back to the boundary between Early–Middle Pleistocene (Gianotti et al. 2008; Serra et al. 2022). The event (and subsequent secondary rockfalls) produced a large talus cone extending down to the valley floor. The slide source area was left covered by a chaotic and highly disaggregated mass of large angular metamorphic blocks, some of which stopped precariously close to the abrupt increase in slope steepness that marks the transition between the toe of the slide and the apex of the talus cone. Continued movements of the slope have led to further destabilization of these frontal blocks, which may slide/topple out of their position and fall at extremely rapid velocity along the talus cone (Bordoni et al. 2018; Licata and Fubelli 2022). In the 1960s, construction of the northern branch of the Turin-Aosta A5 highway was commenced to create a high-capacity connection with the Mont Blanc and Great St. Bernard tunnels at the Italy–France and Italy–Switzerland borders. The highway route was unknowingly located tangentially to the distal edge of the talus cone formed by the Quincinetto landslide. In May 2012, a ~45 m^3 rockfall travelled within a few meters from the road, making local authorities suddenly aware of the impending hazard. Early warning and structural protection alone may not offer definitive solutions to the problem, because: (i) the slide source area occurs high on the slope, is densely vegetated, and can only be accessed by land through a rough hiking trail, hence the frontal blocks can be monitored with limited spatio-temporal resolution; (ii) if one of the largest blocks were to detach, it would attain kinetic energies far in excess of what can be absorbed by any rockfall barrier. Construction of a bypass around the potential runout path is also not feasible in the short term. Risks could instead be minimized with a carefully executed rock reinforcement or rock blasting program, whose arrangement would have to be based on a realistic conceptual model of the blocks selected for stabilization/removal.

Accordingly, here we formulate a series of modelling scenarios regarding the underlying internal structure of the two main unstable blocks at the toe of the slide, and refer to preliminary finite-element analysis to explore corresponding modes of failure. We then exploit 3 years of measurements from an instrumentation network to identify variations in displacement activity and associated triggers. Finally, we co-register two high-resolution point clouds obtained from a terrestrial laser scanner (TLS) and a drone laser scanner (DLS) to extrapolate changes in orientation (dip and dip direction) of moving block faces. By comparing modelled

and actual kinematic styles and damage patterns, we are able to infer which hypothesized representation of the blocks is more consistent with the available field evidence. We illustrate that optimized integration of numerical modelling, long-term displacement monitoring, and repeat topographic surveying can be essential to reduce uncertainty related to the characterization of block instability in "highly data-limited" alpine rock slopes, providing a foundation for the development of hazard mitigation and control strategies.

2 Overview of the Study Site

The bowl-shaped source area of the Quincinetto landslide spreads over $\sim 6 \times 10^4$ m^2 on the E-facing, glacially eroded steep flank of the lower Aosta Valley, ~1 km north of the town of Quincinetto (Northwest Italy). It extends between ground surface elevations 800–1050 m, while the adjacent valley floor sits at elevations below 300 m (Fig. 1a). It is bounded on the west by a ~50 m high sub-vertical rock face, which defines the upper headscarp. The slope is formed by metamorphic rocks belonging to the Eclogitic Micaschists Complex of the Austroalpine domain, consisting of gar-net- and jadeite-rich pervasively foliated mica schists with scattered intercalated lenses of impure marbles and, more rarely, orthogneisses. One of these lenses of dark-colored impure marbles outcrops over a large area of the headscarp and is characterized by a coarse-grained massive structure, in contrast with the fractured appearance of the enclosing rock mass (Fig. 1b). Five discontinuity sets, all striking in a sub-parallel or sub-perpendicular direction with respect to the general slope aspect, provide the conditions for the formation of wedges and rectangular prisms, as evidenced by numerous rockfall scars throughout the steepest mica schist outcrops. Linear slope-scale damage features (lineaments), mapped on a 0.5 m shaded relief derived from aerial LiDAR (SAV, personal communication, January 2022), strike coherently with the orientation of the discontinuity sets (see K1–K5 in Fig. 1c), therefore, suggesting a strong litho-structural control on the development of instability mechanisms. Some of these lineaments correspond to a network of up to 5 m wide tensile and shear cracks that dislocate a secondary scarp of the slide (Fig. 2a). The slope has a distinct glacial imprint. Debris from various rockfall/rockslide sources is extensively mixed up with till, and glacial striations are preserved over some of the less fractured areas of outcropping bedrock, such as the impure marbles that make up the headscarp of the Quincinetto landslide. This indicates that its collapse must have occurred sometime prior to the last pulse of Würmian glacial advance. The distal edge of the talus cone produced by the event, together with landforms of similar origin immediately to the north, has been later fed

by additional rockfalls and reworked by the erosive action of the Dora Baltea River (Fig. 1a).

Traditional geomechanical surveys were conducted by highway contractors in the aftermath of the May 2012 rockfall (SAV, unpublished technical report, 2014). Descriptions and measurements of rock mass and discontinuity properties from these campaigns are in agreement with our observations in the field, and thus served as a reference for the setup of the numerical models herein described. Five scanlines were selected at the toe of the slope, since only impure marbles are accessible at the headscarp of the slide and "blocks" of mica schists composing the secondary scarp—as determined by the aforementioned network of tensile/shear cracks—are back-tilted and relatively rotated. The sampled discontinuities (193) were usually smooth and undulating (JRC = 4–8 from profile gauge testing and visual comparison with ISRM (1978) standard roughness profiles), open (1–5 mm), slightly to moderately weathered (JCS = 25–50 MPa from Schmidt hammer testing, two–three times lower than measurements on fresh rock surfaces), widely spaced (≥ 2 m), highly persistent (≥ 5 m), and dry. They can be tentatively grouped into four sub-vertical/high-angle sets (K1–K4) and one medium-angle set related to the schistosity (K5). High dispersion in orientation complicates the recognition of sets, as depicted by the contour plot of poles to discontinuities in Fig. 3 (equal angle, lower hemisphere projection). Evidence of instability seems more accentuated where K5 dips out of the slope at a suitable angle for basal release. Classification by Bieniawski's (1993) RMR system yielded a value of 65, which is consistent with our visual assessment of a GSI between 55 and 60 according to the equation proposed by Hoek and Brown (1997), but variability in rock mass blockiness and disturbance results in large deviations from these average estimates.

At present, angular blocks up to thousands of cubic meters in volume are chaotically distributed throughout the source area of the Quincinetto landslide (Fig. 1b), with block size having no recognizable spatial pattern. Much of the material is tightly interlocked and visibly detached from the bedrock (Fig. 2b); on the other hand, it is more challenging to evaluate the mechanical interaction with the bedrock of the larger blocks, since these are often encircled by finer debris. Periodic GNSS surveying of 5 rock-bolted threaded steel mounts (ARPA Piemonte, personal communication, April 2022) and satellite interferometric (SqueeSAR) measurements from the Cosmo-SkyMed constellation (TRE ALTAMIRA, personal communication, May 2022) show that the ground surface within the slide boundaries is moving at constant velocities of a few centimeters per year (Fig. 2a). However, information cannot be retrieved from the toe of the slide, where the May 2012 rockfall originated. This sector is delimited at the
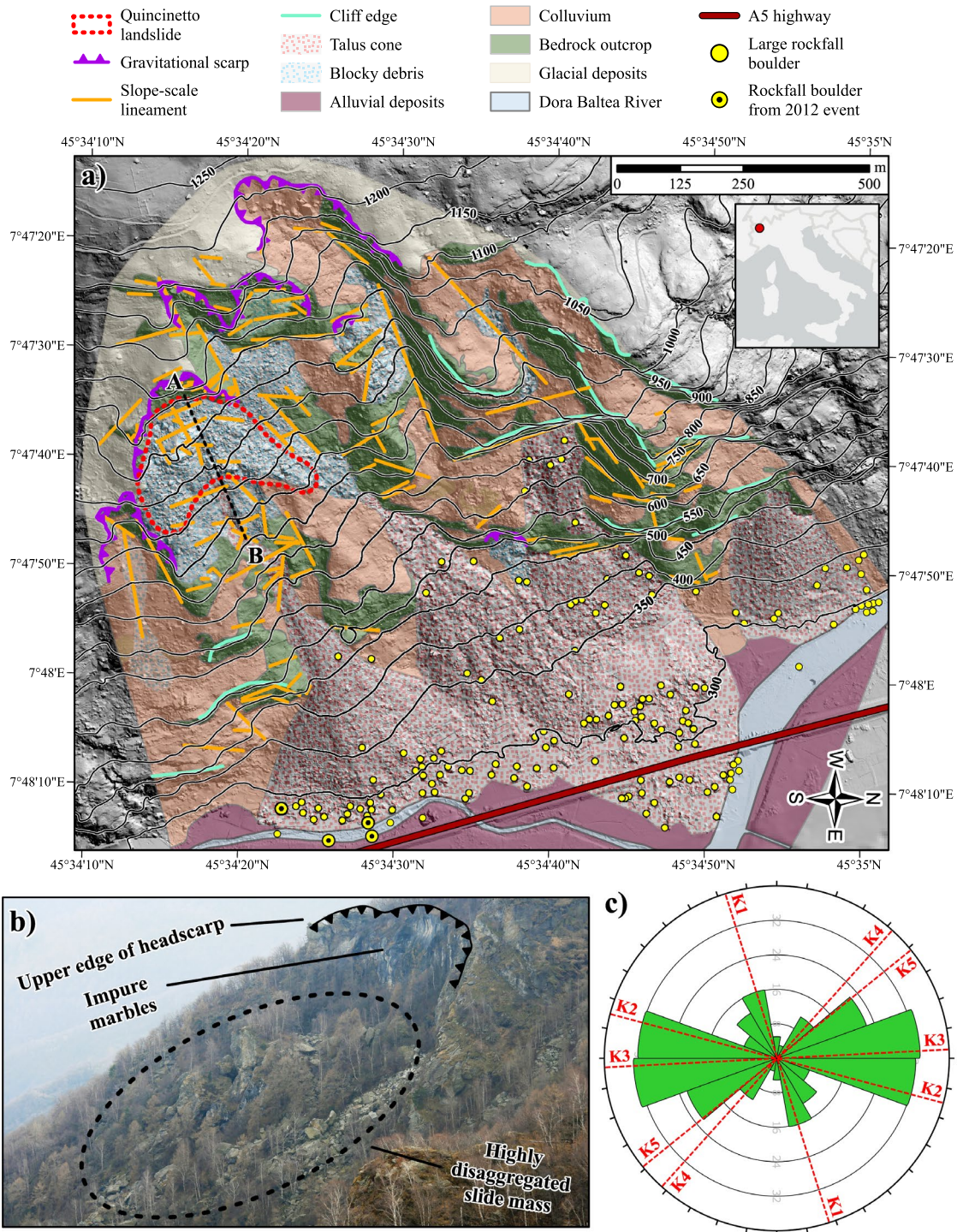
Fig. 1 **a** Geomorphological features on the E-facing flank of the lower Aosta Valley near the town of Quincinetto, showing the location of the A5 highway route and of the slide source area investigated in the present work (as delimited on the basis of satellite interferometric measurements, see Fig. 2). The background shaded relief derives from a 0.5 m aerial LiDAR survey performed in 2012 (courtesy of SAV). Line AB marks the topographic cross section extracted for finite-element modelling (see Fig. 6a). **b** Oblique photograph of the Quincinetto landslide (taken from a panoramic viewpoint at ~1050 m of elevation further to the north, looking south), outlining the ~50 m high sub-vertical headscarp and the highly disaggregated slide mass below. **c** Rosette diagram of slope-scale lineaments. The red dashed lines denote the mean striking direction of the five main discontinuity sets (K1–K5) affecting the Eclogitic Micaschists Complex (see Fig. 3)

Fig. 2 **a** Aerial view of the slide source area. The background orthophoto is the product of a drone-based photogrammetric survey performed in March 2022 concurrently with the DLS survey described in the present work. Satellite interferometric (SqueeSAR) measurements acquired in ascending orbit by the Cosmo-SkyMed constellation (azimuth and incidence angle of satellite look direction: 79.75° and 30.01°) are courtesy of TRE ALTAMIRA. Negative values denote movement away from the satellite. **b** Typical blocky debris within the slide source area. **c** Vertical photograph (taken from helicopter) of the toe of the slide, outlining the trench behind the group of blocks with higher displacement activity
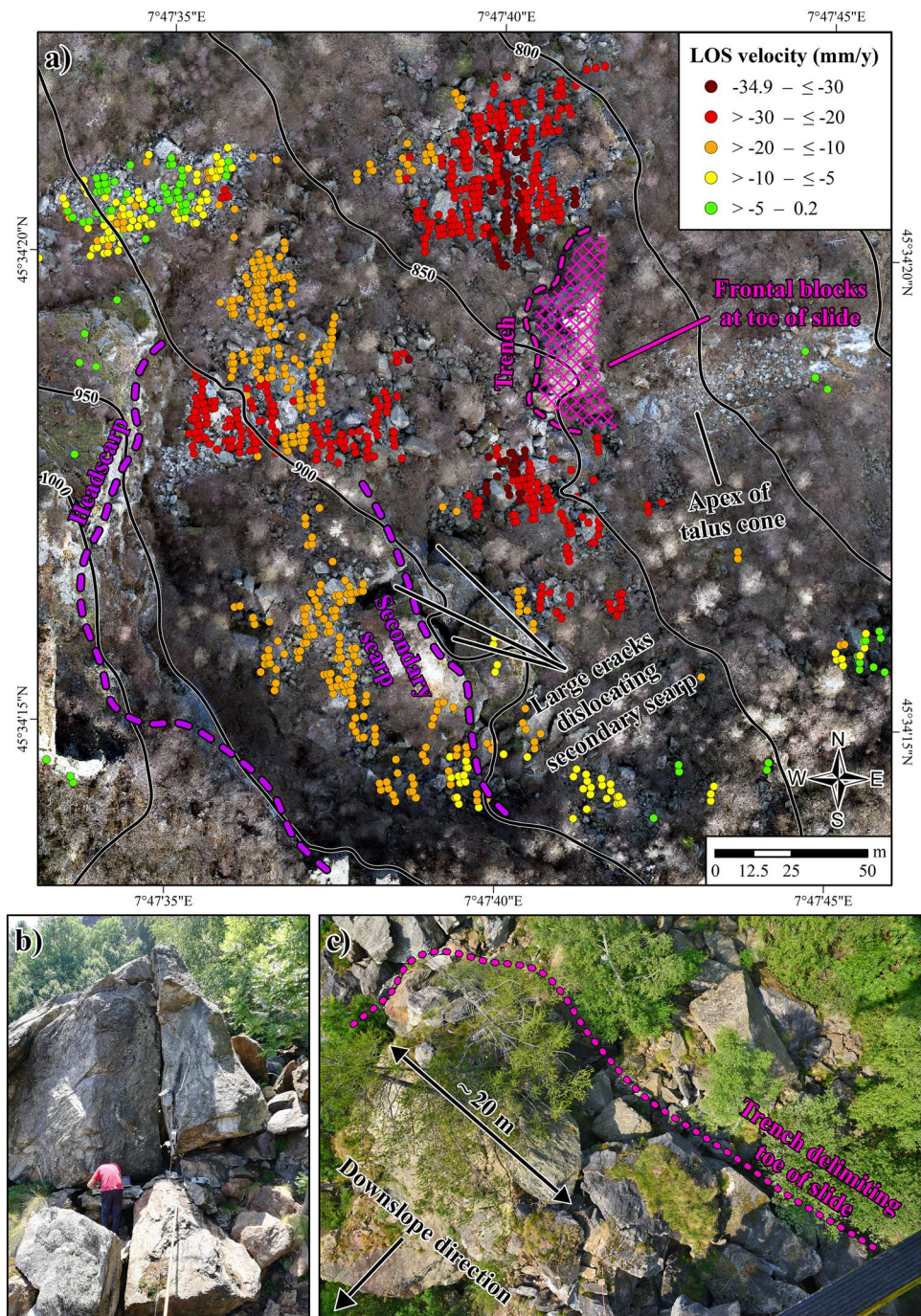
rear by an arcuate trench-like feature ~5 m deep and wide (Fig. 2a, c), which separates morphologically the group of blocks in closest proximity to the apex of the talus cone—the ones with the greatest potential of attaining kinematic release and travelling downslope far enough to reach the highway. The lack of interferometric measurements may be a consequence of too high ground surface velocities for the sensitivity of the technique (Wasowski and Bovenga 2014), while steel mounts for periodic GNSS surveying have not been installed locally for safety concerns.

Figure 4a–e provides photographic documentation of these frontal rock blocks (labelled B1–B5). Blocks B1 and B2 are the largest in the area, with approximate maximum length, width, and height of $20 \times 30 \times 25$ m and $20 \times 20 \times 22$ m, respectively (Fig. 4b). Their volume is estimated in the range $2–5 \times 10^3$ m^3 based on laser scanner data (see 'Methods of investigation'), depending on to what depth their base is projected. They lie, together with B3 (~300 to 400 m^3), in the most advanced position behind the apex of the talus cone. B4 (~15 m^3) and B5 (~200 m^3) are in

Fig. 3 Contour plot of poles to discontinuities from five scanline surveys at the toe of the slope. Red labels identify the average dip/dip direction of the resulting discontinuity sets. Blue crosses identify the orientation of discontinuities measured on block B2 by a geological compass or on point cloud data—some are rough estimates because of hazardous ground and poor point cloud density. The pink cross identifies the orientation of a remarkable sub-planar structure outcropping at the apex of the talus cone (colour figure online)
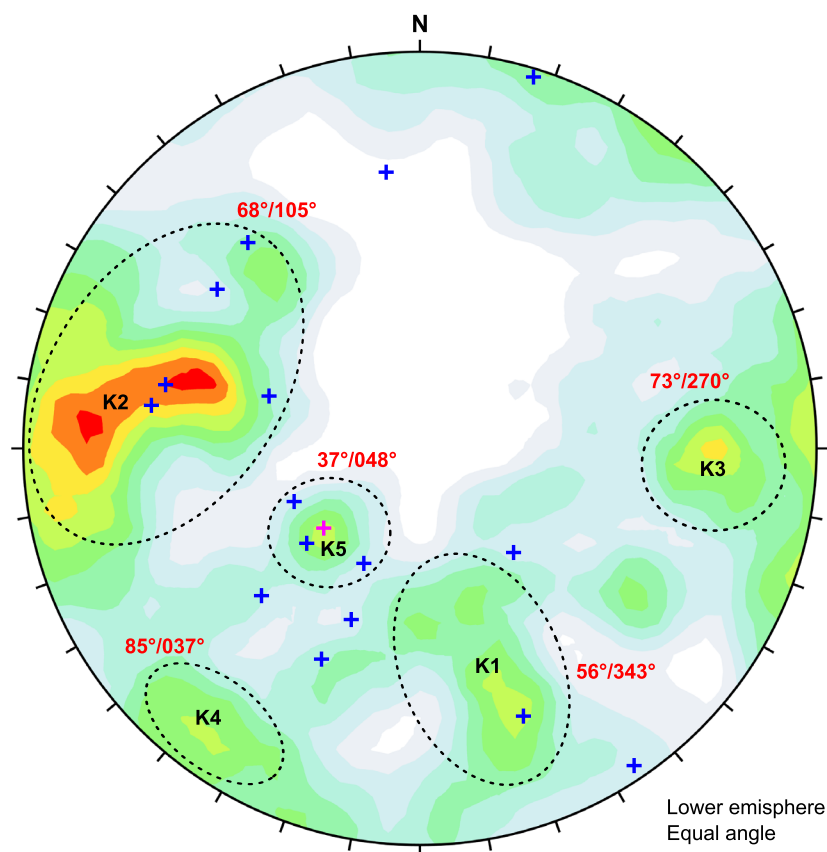
contrast visibly detached from the bedrock: they lie across the trench that delimits the toe of the slide, with B5 leaning against B4 and B4 leaning against B2 (Fig. 4c). The bottom of the trench, as well as the ground between B1 and B2, is filled with variably sized blocky debris of unknown thickness.

In light of their precarious position, large volume, and pronounced height, blocks B1 and B2 pose the highest concern to highway operations, and, therefore, are the focus of the present work. They are also important for the overall stability of the toe of the slide, forming a barrier that prevents the mobilization of surrounding debris. Their surface appearance is not homogeneous: lower parts typically have massive structure, whereas upper parts are heavily damaged in places with a contribution of brittle rock fracture (Figs. 4d, 5b), likely promoted by the initial collapse and continued slow deformation of the slope. Particularly undamaged areas tend to jut out of the block faces. At the very top of the blocks, the rock mass is partially disintegrated (Fig. 4d). In addition, B1 is intersected to the rear by an almost 1 m wide, undulating sub-vertical tensile fracture (Fig. 4e). Both B1 and B2 are largely unconfined on the sides, but for reasons stated above neither visual inspection

or core logging may assist in establishing basal boundaries. These uncertainties about the underlying internal structure of the blocks inhibit the design of countermeasures aimed at their stabilization or removal.

3 Methods of Investigation

The investigation of rock blocks B1 and B2 was undertaken by assuming that their underlying internal structure is reflected by their kinematics. More specifically, the fundamental questions to be addressed are: whether they have significant cohesive continuity with the bedrock, or their strength is rather dictated by friction along a through-going basal rupture surface; and whether the brittle fracture damage observed in places is confined to the exterior of the block faces, or is pervasive. While the majority of the other blocks accumulated on the slide source area are part of a chaotic deposit with no mechanical interaction with the bedrock (Fig. 2b), the same conclusion may not pertain by analogy to B1 and B2. It would imply that B1 and B2 came to rest on discontinuous block-to-debris contacts right on the steep edge of the talus cone

Fig. 4 **a** Detailed aerial view of the frontal rock blocks. Note that sub-verticality of some block faces (especially at B1) causes perspective distortion in the orthophoto. **b** Oblique photograph (taken from helicopter, looking upslope) of blocks B1, B2, and B5. **c** Close-up photograph (taken from S2, looking upslope) of blocks B4 and B5. **d** Rock mass disintegration at the top of B1. **e** Sub-vertical tensile fracture to the rear of block B1
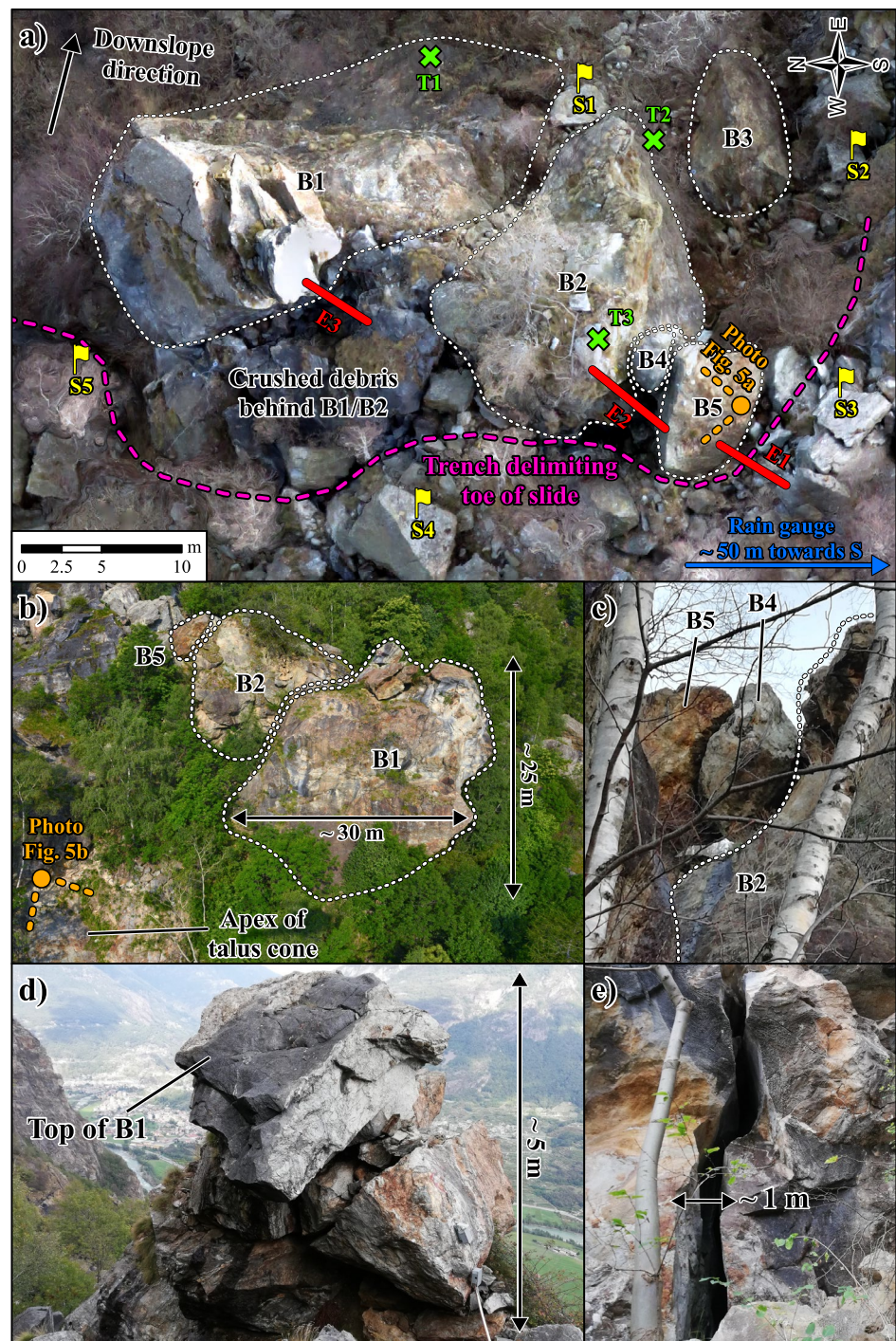
when (or after) the slope initially collapsed, notwithstanding the momentum gained under a condition of complete kinematic release. This is arguably improbable to have occurred owing to their dimensions and arrangement. A mechanical interaction with the bedrock can also be inferred by the stereographic projection in Fig. 3, where blue crosses represent the orientation of 15 highly persistent discontinuities measured—sometimes roughly—on block B2 by a geological compass or on point cloud data (described later in this chapter). Most measurements can be associated with the more frequent sub-vertical set K2 and the schistosity-related set K5.

Fig. 5 **a** Sub-planar structure outcropping at the apex of the talus cone. **b** Evidences of brittle fracture damage on the uphill-facing side of block B2 **c** Close-up photograph of the upper S-facing lateral side of block B2 (taken from block B5, looking north), showing the anchoring points of tiltmeter T3 and extensometer E2 (downslope direction is to the right of the photograph). **d** Oblique photograph (taken from helicopter, looking downslope) of the lower slide source area and talus cone, highlighting the relative location of the GBInSAR installation site and of the highway at risk for rockfalls

3.1 Preliminary Numerical Modelling

Applications of numerical modelling to the study of rock slopes commonly make reference to situations, where the mode of failure is well-constrained by large amounts of field and monitoring data. When data are limited, as

recommended by some authors (Eberhardt 2008; Stead and Coggan 2012), numerical modelling may be conducted as a preliminary analysis to anticipate how failure may develop. This can indicate the critical parameters to investigate, allow the selection of an appropriate strategy to measure those parameters, and eventually help constrain

the interpretation of collected data. We used the commercial 2D finite-element code RS2 (Rocscience 2023) to recreate the following hypothetical representations (scenarios) of B1 and B2:

1. B1 and B2 are mostly undamaged blocks separated from the bedrock by a persistent planar basal joint;
2. B1 and B2 are mica schist outcrops having full cohesive continuity with the bedrock;
3. B1 and B2 are blocks de facto separated from the bedrock due to pervasive internal damage.

Justification for scenario 1 comes from a remarkably subplanar structure dipping at ~35° (dip direction ~50°, see pink cross in Fig. 3) on the very apex of the talus cone, ~25 m to the southeast of block B2 (Fig. 5a). Visual inspection, performed by use of rock climbing equipment, did not reveal obvious heterogeneities in weathering or roughness along the surface, suggesting that this was not involved as basal release of the recent May 2012 rockfall—as trees were damaged by the event only on lower slopes, the source block must in any case have been located somewhere in the immediate vicinity. Scenario 1, therefore, reproduces the existence of such a structure at the base of blocks B1/B2; scenario 2 models the opposite condition, namely, that B1/B2 are actually spurs of bedrock that remained in place after collapse of the slope; and scenario 3 considers deformation to be mechanically controlled by randomly oriented brittle fracture damage, having the pre-existing rock mass structure (as determined by the discontinuity sets and possible basal surface) effectively been suppressed.

Although exploiting a continuum small-strain formulation, the adopted code can explicitly account for the presence of joints by means of Goodman interface elements (Goodman et al. 1968; Ghaboussi et al. 1973; Beer 1985). It has proved versatile in capturing the behavior of discontinuous rock masses, from individual block movement to continuum-like mechanisms and combined modes (Hammah et al. 2008;

Agliardi et al. 2013). Since the two blocks under investigation have equivalent shape and size, we extracted a single topographic cross section extending from the headscarp to the apex of the talus cone and passing through B2 (see Fig. 1a for the planimetric location). Stress–strain computations involved a shear strength reduction analysis applied simultaneously to the rock mass material and explicit joint elements (when present). This incrementally reduces the assigned shear strength parameters until excessive displacements cause the solution of the force equilibrium equations to no longer converge, at which point failure is assumed to initiate (Hammah et al. 2005). The 2D domain was discretized into a graded mesh of six-noded triangular finite elements. Considering the strong lithological heterogeneity in the headscarp area and the lack of any subsurface information, boundary conditions were imposed to confine displacements within the cross-sectional length between the trench and the apex of the talus cone. Differences between modelling scenarios were thus emphasized by preventing deformation on the steep higher slopes from affecting kinematics and damage at the toe of the slide. Ignoring the interplay between local- and slope-scale dynamics in the simulations may be acceptable given the well-developed state of the trench and the discrete nature of blocks B1/B2. The horizontal stress ratio was left at the default value of 1 (exploratory model runs proved insensitive to the use of other values).

The mechanical properties of the rock mass (Table 1) were assigned by converting the estimated RMR rating into values of cohesion and friction angle, as derived proportionally from the ranges given by Bieniawski (1993) for the class of "good rocks". The associated tensile strength was set to 0.1 MPa, in line with calculations by Hoek and Brown (1997) for schists of similar quality and with the recurrent evidences of brittle fracture damage. The Young's modulus was derived from the equation proposed by Bieniawski (1978), and assumed typical values for metamorphic rocks were used for the Poisson's ratio and unit weight. We then

Table 1 Rock mass and joint properties inputted into the RS2 models

Property	Rock mass (Mohr–Coulomb) $\tau = c + \sigma_n \tan \varphi$	Joints (Barton–Bandis) $t = \sigma_n \tan[\varphi_r + JRC \log_{10}(JCS/\sigma_n) + \varphi_r]$
Unit weight	0.026 (MN/m^3)	–
Young's modulus	29.6 (GPa)	–
Poisson's ratio	0.25	–
Cohesion	0.32 (MPa)	–
Friction angle	37.7 (°)	30 (°)
Tensile strength	0.1 (MPa)	–
JCS	–	44.7 (MPa)
JRC	–	6
Normal stiffness	–	10^5 (MPa/m)
Shear stiffness	–	10^4 (MPa/m)

acquired roughness and rebound measurements on the sub-planar structure at the apex of the talus cone by means of a profile gauge and a Schmidt hammer. The obtained JRC and JCS—the former being corrected for scale according to Barton's (1981) amplitude/length method—fall within the range of estimates made during the scanline surveys in 2012, and were thus uniformly assigned to every joint element inputted into scenarios 1 and 3 together with assumed typical values for the residual friction angle and normal/shear stiffness (Table 1). The aperture of joints induced by brittle rock fracture in blocks B1 and B2 is often extremely wide, generating in some cases complete separation of rock mass pieces (Figs. 4d, 5b). As such, joint strength in scenario 3 may be deemed overestimated if the same properties of scenario 1, which involve apparent cohesion related to joint roughness, are used. If joints in scenario 3 were instead assigned true cohesion and tensile strength in a Mohr–Coulomb framework to account for limited persistence, the formulation of the model would in essence approximate the hypothesis of a bedrock spur made in scenario 2. A simplified parametrization is reasonable in the context of our study, because the shear strength reduction analysis is not here focused upon retrieving a reliable slope factor of safety, but upon exploring potential kinematic styles and damage patterns of blocks B1/B2 at failure. For example, conversion of Hoek–Brown rock mass parameters is expected to yield higher equivalent Mohr–Coulomb strength and a lower Young's modulus, but exploratory model runs based on ranges of GSI = 55–60, uniaxial compressive strength of the intact rock σ_{ci} = 70–90 MPa (from Schmidt hammer testing on fresh rock surfaces), and assumed typical values for schists (Hoek 2023) of the constant m_i = 9–15, have shown differences to strictly concern outputted factors of safety and not overall behavior.

3.2 Geotechnical Monitoring

We implemented a geotechnical instrumentation network to measure the displacements of the frontal rock blocks. To this aim, spatial redundancy was enhanced through combined use of remote sensing and in situ monitoring. Serious limitations are in fact posed to remote sensing monitoring by occlusion effects arising from the rugged topography and the vegetation growing around the blocks (Fig. 4b); similarly, instruments that operate in physical contact with the blocks could only be placed in a few accessible spots. The network is composed of three wire extensometers, three biaxial tiltmeters, a non-heated tipping bucket rain gauge, and a Ground-Based Interferometric Synthetic Aperture Radar (GBInSAR). The measurements presented in this study refer for most instruments to a 3-year span, from June 2019 to May 2022.

Figure 4a identifies the location of the extensometers, tiltmeters, and rain gauge, all equipped with an automatic data logger to acquire measurements at a frequency of 20 min. The two ends of extensometer E1 were anchored on the S-facing lateral side of block B5 and the N-facing lateral side of another block on the opposite side of the trench. This choice was made based on the notion that the well-developed extent of the trench and the lack of coherent SqueeSAR targets at the toe of the slide (Fig. 2a) are indeed determined by ongoing accelerated movements with respect to the rest of the slide source area. Extensometer E2 connects the N-facing lateral side of B5 with the S-facing lateral side of B2 (Fig. 5c), whereas extensometer E3 connects the S-facing lateral side of B1 with one of the blocks in the accumulation of crushed debris at the bottom of the trench. Steep hazardous ground prevented us from connecting B1 or B2 to anchoring points outside the trench. As for the other instruments, tiltmeter T1 was installed at the base of the downhill-facing side of B1; tiltmeter T2 at the base of the downhill-facing side of B2; tiltmeter T3 at the top of the S-facing lateral side of B2, next to the anchoring point of E2; and the rain gauge on the top side of a flat block behind the trench.

The GBInSAR was installed in the valley floor at a Line-Of-Sight (LOS) distance of about 1.3 km from the slope sector of interest (Fig. 5d, see 'Results' for the planimetric location of the installation site). This technique is widely recognized as one of the most advanced for remote sensing monitoring of mountainous rock slopes (Atzeni et al. 2015; Woods et al. 2020; Carlà et al. 2019, 2021). In summary, the main component is a continuous-wave step-frequency radar that transmits in K_u band (center frequency ~ 17 GHz) and moves along a mechanical linear rail to create a synthetic aperture. Range and azimuth synthesis of complex images are obtained by coherently summing signal contributions relative to different antenna positions and microwave frequencies (Casagli et al. 2010). LOS displacement of the targets (i.e., radar pixels) are then associated with sub-millimetric accuracy to the phase shift of the back-scattered signal between two or more acquisitions. In the employed configuration, blocks B1 and B2 are illuminated on their downhill-facing and lateral sides by about a dozen radar pixels having range and azimuth resolution of 2.5 × 4.1 m—in 'Results', we comment on the displacements of two pairs of representative highly coherent pixels named P1a–P1b (block B1) and P2a–P2b (block B2). Radar images were averaged over a rolling time window of 1 h to minimize decorrelation effects arising from the paucity of nearby stable, non-vegetated areas that could be exploited for compensation of the atmospheric phase screen (Luzi et al. 2004; Monserrat et al. 2014; Pieraccini and Miccinesi 2019).

3.3 TLS/DLS-Based Topographic Surveying

We conducted two high-resolution topographic surveys of the frontal blocks and surrounding slope areas in September 2019 and March 2022. In the first survey, we operated a RIEGL VZ1000 from the GBInSAR installation site and other five viewpoints at a close range from the blocks to maximize the number of faces reached by the laser pulse (see S1–S5 in Fig. 4a for the scanning locations at the toe of the slide). The second survey in contrast required a single scan scene thanks to use of a RIEGL VUX–1UAV (not previously available to us) on an ad hoc drone prototype (Rossi et al. 2018). An inertial navigation system and a GNSS receiver are embedded into this DLS device to automatically correct measurements acquired during flight. The drone path was planned to maintain a fixed airspeed of 5 m/s and a fixed flight height of 120 m above ground level.

Proprietary RIEGL post-processing packages allowed us to georeference all point clouds with centimeter accuracy by means of GNSS-surveyed ground control markers. Vegetation was removed by applying the built-in 'terrain filter' tool and later refining the result manually. We attained a mean density of the DLS-based point cloud of 247 units/m^2, compared to 240 units/m^2 of the final TLS-based point cloud (derived by merging the different scan scenes from the valley floor and toe of the slide). These were then co-registered with the 'point pairs picking' tool of the CloudCompare (2023) software package. The tool is conceived to precisely align two point clouds through manual matching of at least three tie point pairs (i.e., points that are assumed to have the same coordinates in both entities), overcoming the limitations inherent to classic iterative closest point routines when slope movement directions are strongly heterogeneous (Kenner et al. 2022). At the study site, this procedure is facilitated by the sharp-cornered outline of the blocky debris within the slide mass boundaries. Tie points were evenly sampled from the slope area behind the trench. Satellite interferometric measurements denote local cumulative displacements of 6–9 cm for the period between the surveys (TRE ALTAMIRA, personal communication, May 2022), up to one order of magnitude lower than the values recorded at B1, B2, and B5 (see 'Results'). Shifts of the frontal blocks from one point cloud to the other will, therefore, be attenuated, but still observable. Moreover, we assume that such slow slope-scale deformation reflects some form of deep-seated instability, hence we exclude rotations or otherwise complex movements of individual blocks behind the trench that could induce significant distortions during co-registration.

4 Results

4.1 Potential Failure Kinematics and Damage Patterns

Figure 6a outlines the main geomorphological features along the extracted topographic cross section and the area at the toe of the slide where boundary displacements were allowed in numerical analyses. Model outputs were evaluated qualitatively based on the geometry of the deformed domain mesh and the distribution of mesh elements yielded in tension at the critical strength reduction stage of each simulated scenario. To do so, the mesh was displayed by scaling the deformation to a fixed factor of 5000 (i.e., 1 mm of calculated displacement is magnified to 5 m in the deformed domain mesh). Mesh elements yielded in shear are omitted from Fig. 6b−d for better visualization, as they overlap with some of the mesh elements yielded in tension and, only when a through-going basal joint is not included, are also located in a small area at the front of B2. Prevalent tensile yielding is consistent with field evidences and the expected behavior of the investigated rock mass.

Examining the model simulations, scenario 1 shows the expected outcome (Fig. 6b). Slip is initiated along the through-going basal joint (drawn with an inclination of 35° by analogy with the dip of the sub-planar structure at the apex of the talus cone) when its shear strength is sufficiently reduced, and B2 is consequently displaced without rotation or internal deformation. Yielding in tension is observed near the back of the block at shallow depth, and especially concentrates in mesh elements adjacent to the area of the trench.

In scenario 2, no explicit joint elements are built into the model domain and B2 is regarded as an outcropping spur of undisturbed bedrock. Mesh deformation points to a slight forward rotation (toppling) of the rock spur leading to its failure (Fig. 6c). Mesh elements yielded in tension are more numerous than in scenario 1, forming an almost continuous zone that stretches from the rear to the frontal face of the rock spur. Bulging at the toe is interpreted as an artefact of the restraining boundary conditions imposed downslope.

To simulate the pervasive internal damage of block B2 in scenario 3, that is to reproduce a condition, wherein randomly oriented brittle rock fracture (Figs. 4d, 5b) has mechanically suppressed any strength anisotropy related to the pre-existing rock mass structure, a joint network composed of a medium-regular Voronoi tessellation (maximum joint length 1.5 m) was incorporated into the model. This tessellation scheme randomly subdivides the domain area of interest into non-overlapping convex polygons, whose bounding segments are regarded as joints. When the model is brought to failure, the block structure collapses by showing more pronounced forward rotation than in scenario 2
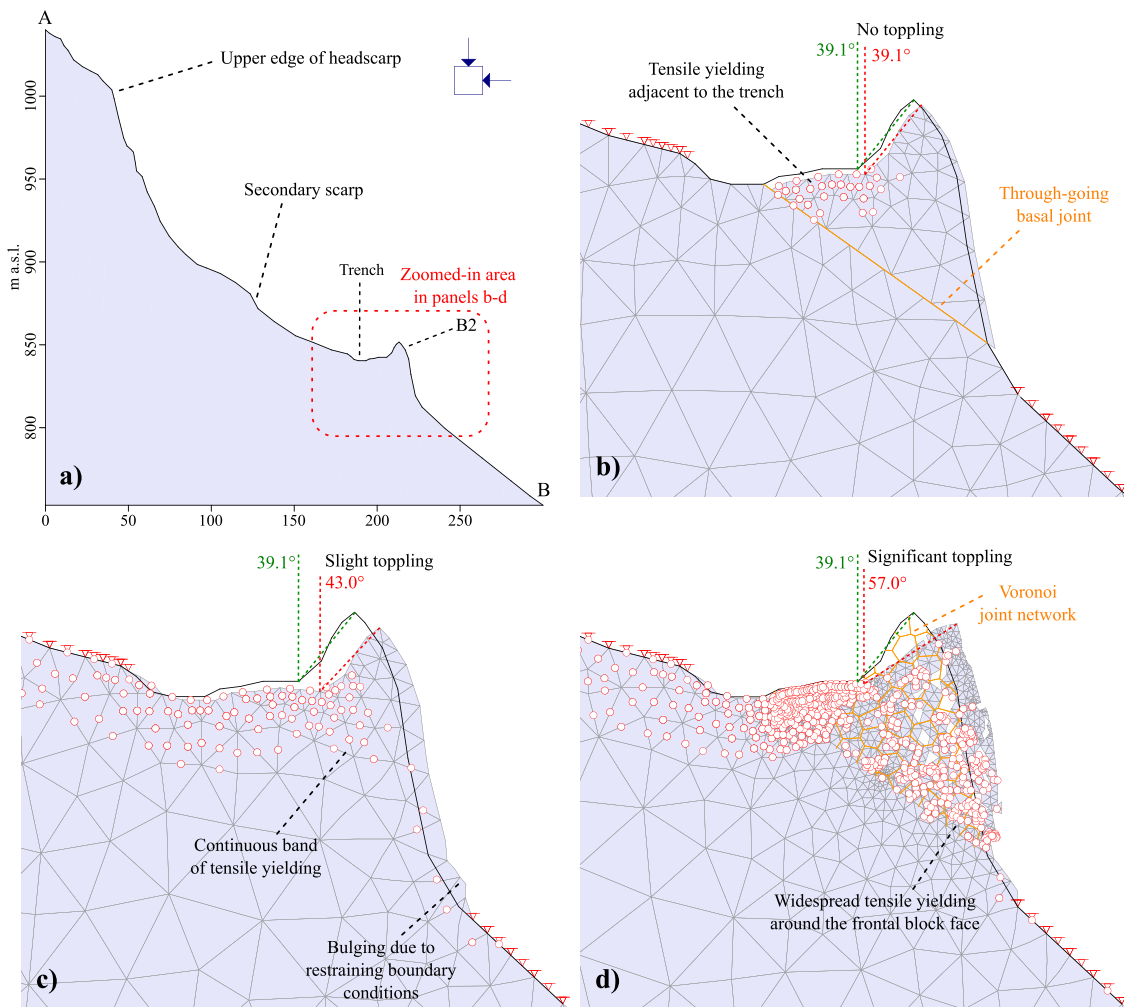
Fig. 6 Preliminary finite-element analysis of potential modes of failure of the frontal rock blocks: **a** selected topographic cross section passing through B2 (see line AB in Fig. 1a). **b, d** Outcomes of modelling scenarios 1 (through-going basal joint), 2 (spur of bedrock), and 3 (pervasive damage within the block), respectively. Triangular "pin" symbols indicate restrained boundary nodes in the *x–y* directions; note that these continue further to the left and right of the zoomed-in view, including the lateral and basal boundaries of the model

(Fig. 6d). Yielding in tension is widespread, as the main rock volume breaks into smaller pieces that are progressively released from the frontal block face.

4.2 Variations of Displacement Activity

Figure 7a–d details the cumulative time series measurements acquired by the instrumentation network. The displacement curves of the extensometers all show a distinct sequence of acceleration and deceleration phases. The largest cumulative displacement in absolute value (~30 cm) is as expected recorded by E1, this being the only extensometer that could be installed across the full width of the trench. E3 records approximately one fifth of the displacements of E1, but this could partly be ascribed to the anchoring block at the bottom of the trench being to some extent destabilized by movement of B1. E2 records negative displacements (i.e., shortening of the cable), implying either release of block B4 from an interlocked position between blocks B2 and B5, relative rotation of block B2 and/or block B5 around the vertical (yaw) axis, or a combination thereof. The trend of measurements from E1 also agrees closely with that of radar pixels P2a–P2b. This substantiates field observations that blocks B4/B5 are detached from the bedrock and lean against block B2, which, therefore, directly controls their stability. Extensometer measurements at E1 can in this sense be considered as a proxy for the displacements of B2. Repeated agreement between extensometer and radar measurements occurs at B1, where pixels P1a–P1b have the same displacement trend as E3—and again report comparatively larger cumulative values, although these are confirmed to be lower than at B2 (see cumulative displacement map in Fig. 8). Tiltmeter
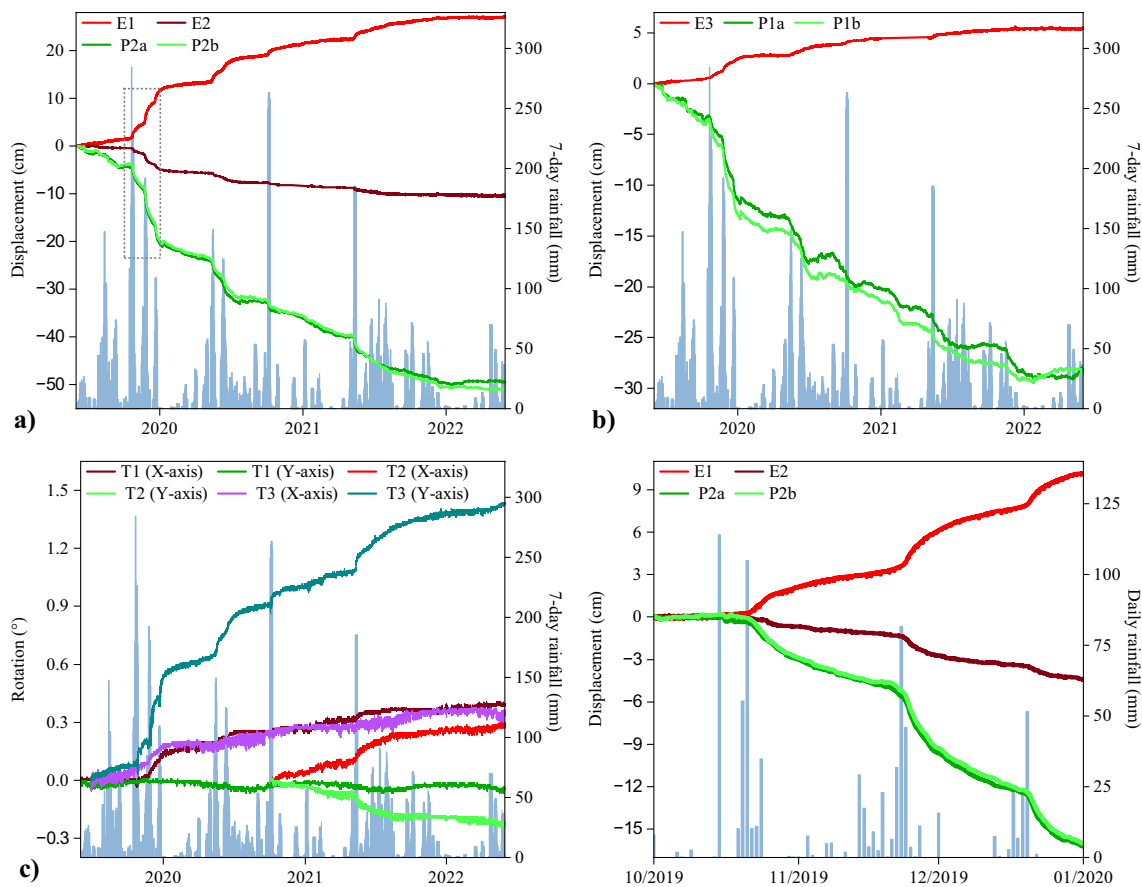
Fig. 7 a, b Cumulative time series measurements acquired by the extensometers and GBInSAR. The dashed black rectangle in (a) delimits the period detailed in (d). **c** Cumulative time series measurements acquired by the tiltmeters. **d** Displacements measured by extensometers E1–E2 and radar pixels P2a–P2b between October–December 2019. In (**a–c**), rainfall measurements are cumulated on a weekly basis for better visualization

measurements at T1 and T2, installed at the base of B1 and B2, do not show a sequence of acceleration and deceleration phases, such as the extensometers and radar points, or a definite rotation around one of the axes (measurements at T2 started in October 2020 due to technical malfunctions). The opposite is observed at T3, installed near the top of B2, where alternating accelerations and decelerations are detected around the *Y*-axis (cumulative value 1.5°), with positive values denoting rotation towards the south.

Rain gauge measurements highlight that such increases in displacement activity were triggered by rainfall. However, there is no straightforward correlation between the amount of rainfall in a "rainfall event" (herein defined as any period characterized by at least 24 mm of rainfall in 24 h and dry spells, if present, shorter than 12 h) and the ensuing peak of velocity recorded at extensometer E1 (Fig. 9). Rainfall events of similar magnitude are in fact associated with markedly different values of peak velocity—this remains valid if reference is made to rainfall intensity/duration. Major reactivations of block B2 were invariably concomitant with

rainfall events that involved the higher rainfall amounts in the data set, but also with more moderate rainfall events that occurred during the tail of a previous reactivation (e.g., see Fig. 7d, highlighting the displacement–time curves and rainfall measurements for the period October–December 2019). Further evidence for this behavior is provided by color mapping the data points in Fig. 9 according to the "background velocity" recorded at extensometer E1, namely, the instantaneous velocity at the onset of the corresponding rainfall event. Data points implying negligible background velocities (i.e., no ongoing movements when rain starts to fall) align in the lower part of the plot, whereas the others are less closely distributed and broadly imply progressively higher background velocities going upwards on the *y*-axis. This variability is captured by explicitly inputting in a 3D plot the rainfall amount and corresponding peak/background velocities for each rainfall event (Fig. 10a): data points are well-fitted to a polynomial surface, whose shape symbolizes that the negative impact of rainfall on the stability of B2 is escalated by high background velocities (the December 2019

Fig. 8 Cumulative displacement map acquired by the GBInSAR between June 2019 and May 2022. Negative values denote movement towards the radar. In the inset, note that the amount of displayed measuring points is greater than the actual amount of radar pixels identified over blocks B1 and B2 (the light-colored rectangles illustrate the approximate coverage of the four radar pixels selected for analysis). This mismatch derives from resampling and projection of data on the TLS-based point cloud acquired from the installation site
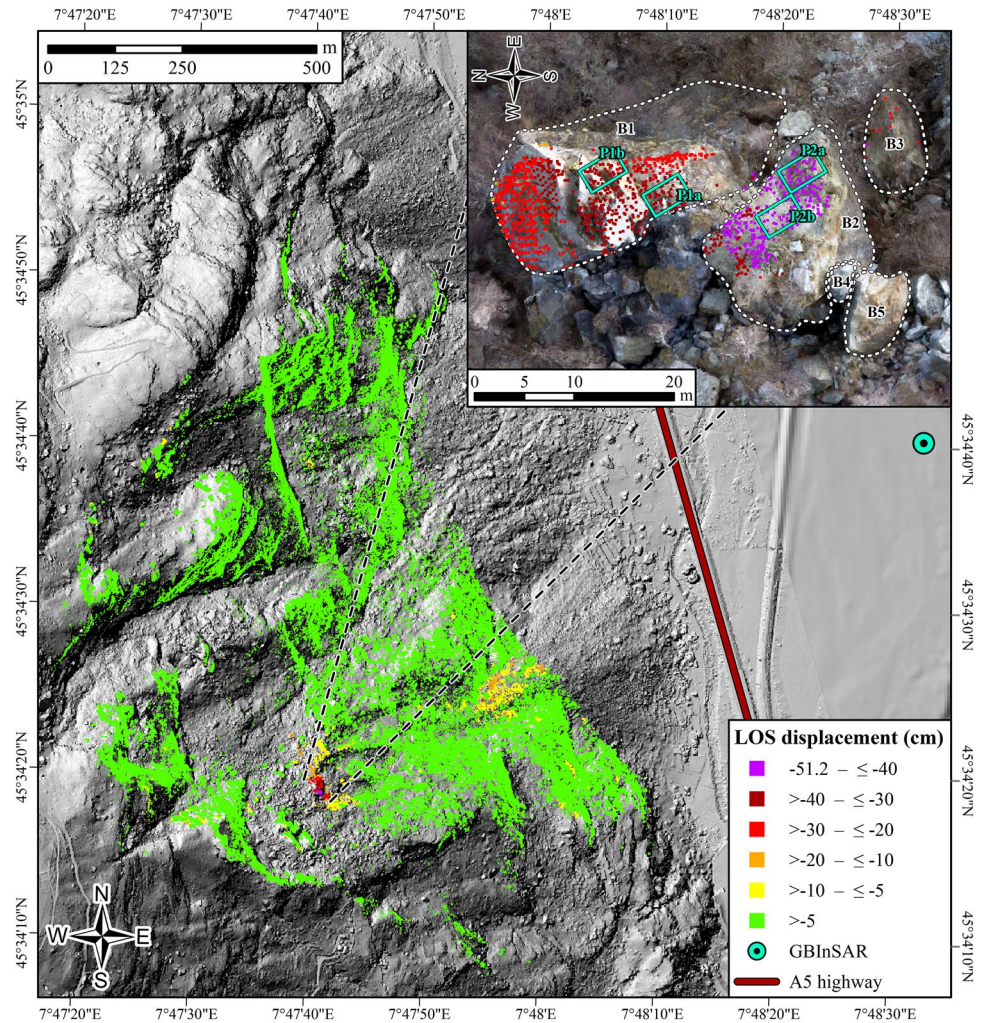
data point was left out of the regression, since it visibly deviates from the dominant trend, as discussed later). Equivalent results are obtained from extensometer E3 (Fig. 10b), although the plot is populated by fewer data points due to the lack of a measurable response of block B1 to rainfall events of lower magnitude.

4.3 Orientation of Moving Block Faces

Given their shape and material, we can expect the investigated blocks to change position in space by rigid transformation; in other words, intact block faces will translate and/or rotate without internal deformation. Differential movements could still occur within a block face if damage is pervasive enough to generate highly independent sub-volumes of rock (scenario 3). To fully assess kinematic styles, we first isolated the frontal blocks one by one in the merged TLS-based point cloud (Fig. 11a) and in the DLS-based point cloud (Fig. 11b). We then identified clusters of points belonging to the same block face and appearing coherently in both

surveys. With the help of photographs taken in the field, we visually inspected each cluster to filter out exceedingly rough or fractured areas and finally derived best-fitting planes in CloudCompare. By observing how planes fitted to different faces of a rock block have changed dip and dip direction, we can determine whether translational or toppling movement is globally to be invoked.

Figure 12a summarizes the results of the analysis for block B2. Homologous pairs of best-fitting planes were derived from its uphill-, downhill-, S-facing lateral sides, and top side, with a relative shift between entities in the order of 60 cm (Fig. 12b). This value—an underestimation of the actual absolute displacement, since the point clouds were co-registered by assuming complete stability behind the trench—is consistent with GBInSAR measurements (Fig. 8), which are downscaled to the LOS. We find no evidence of toppling: the S-facing and top sides preserve their original dip; a calculated increase of 1° on the downhill- and uphill-facing sides may not be considered relevant either. In general, we noted that user selectivity in the manipulation
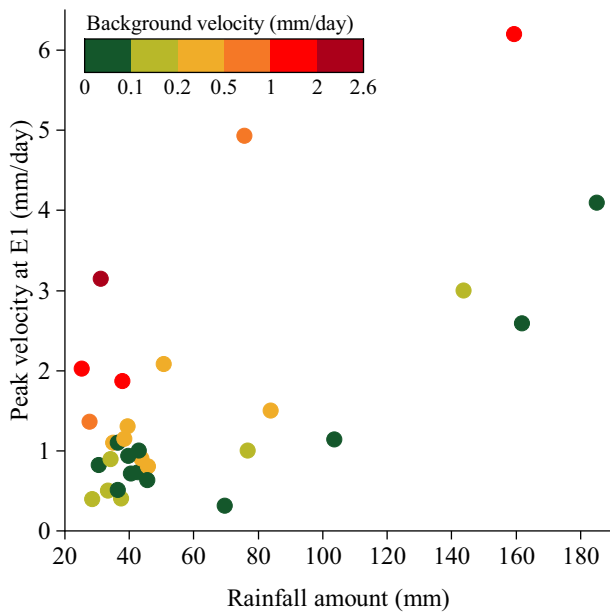
Fig. 9 Plot of total rainfall amount in a "rainfall event" versus the ensuing peak of velocity recorded at E1. Values of instantaneous velocity are calculated through differentiation of the cumulative displacement measurements in Fig. 7a on a 24-h basis (i.e., by subtracting each cumulative displacement measurement from the measurement acquired 24 h prior)

explained by the smaller gap between the cumulative LOS displacement measured at radar pixels P1a–P1b (~25 cm from September 2019 to March 2022 against ~50 cm at radar pixels P2a–P2b, see Fig. 7a, b) and the baseline slope-scale displacement that was neglected for co-registration of the point clouds, and is again proof that B1 has recently been less prone to instability than B2. To demonstrate the ability of the procedure to detect changes in the orientation of moving block faces, we depict the results for block B5 in Fig. 12c. A homologous pair of best-fitting planes was derived from its sloping top side, revealing a notable increase of 7° in dip direction. This is kinematically justified in view of the block-to-block contacts along the northeastern and southeastern corners, respectively, with B4 and another large block behind the trench: as B2 (and by extension B4) moves downslope, the fixed constraint on the southeast acts as a pivot point around which B5 is forced to rotate clockwise. The above is compatible with the negative displacements recorded at extensometer E2.

5 Interpreted Mechanisms of Block Instability

The presented analysis workflow provides important insights into the two main unstable rock blocks at the toe of the Quincinetto landslide. Displacement monitoring and topographic surveying have in many cases been used as input or constraint to the analysis of rock slope stability (Francioni et al. 2018). Here, we used an alternative approach, whereby preliminary 2D numerical modelling was instrumental into discerning variations in kinematic style and damage pattern for a range of scenarios concerning the underlying internal structure of the blocks. This guided us in the acquisition of suitable data to substantiate one among such hypotheses—we stress that, site conditions permitting, it is always preferable to incorporate direct information on the mechanisms of

of source clusters (e.g., decision to retain or filter out areas of a block face that are arguably too rough or fractured, or where a disparity exists between point cloud densities) was unlikely to change the orientation of fitted planes by more than two degrees. Dip directions remain basically unaltered as well, indicating a constantly oriented translational movement of the block.

Three pairs of planes were derived from the uphill- and downhill-facing sides of block B1, but the relative shift between entities is much more subtle (~10 to 15 cm, with changes in dip or dip direction up to 1°). This can be

Fig. 10 3D scatter plot of rainfall amount, background velocity, and peak velocity characterizing rainfall events in the data set: **a** data from E1 (block B2); **b** data from E3 (block B1)
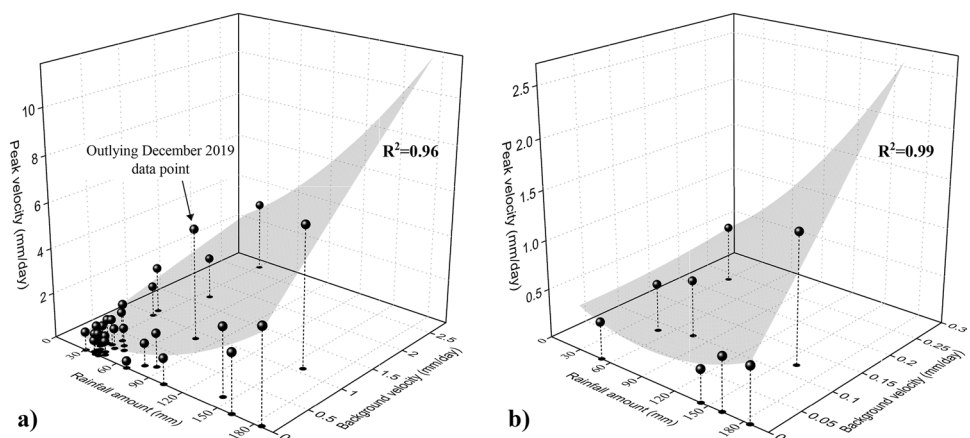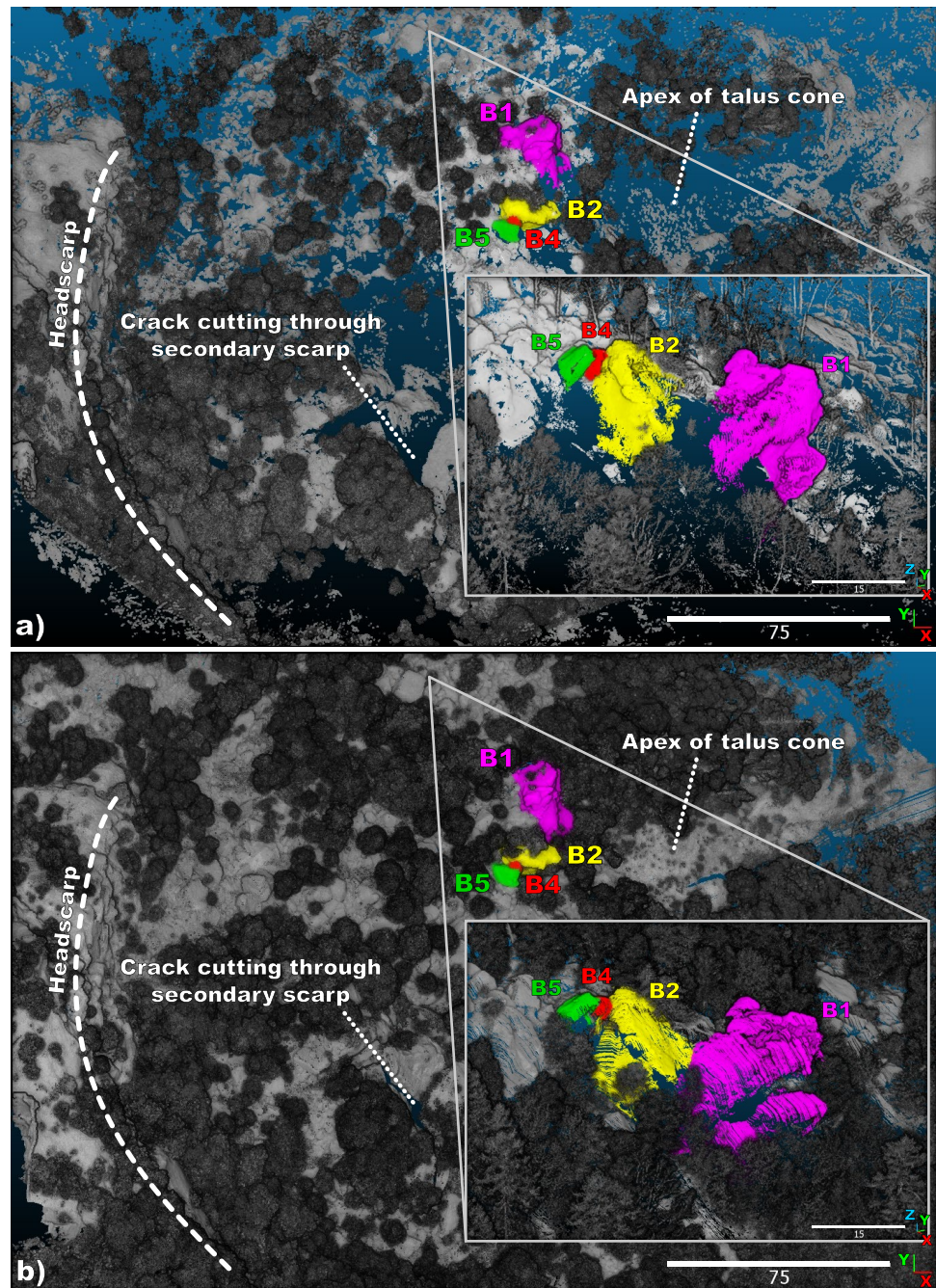
Fig. 11 Overview of the **a** merged TLS-based point cloud and **b** DLS-based point cloud, prior to removal of vegetation and co-registration. In both panels, blocks B1, B2, B4, and B5 are depicted with distinct colors (B3 is hidden by vegetation at the base of B2), whereas gray tones in the rest of the point cloud depend on laser return intensity


instability into numerical analyses based on a thorough rock slope characterization.

Table 2 lists the main sources of model uncertainty imposed by the "highly data-limited" nature of the site. These meant that several simplifications had to be made in constructing the models, most notably the consideration of a 2D domain, dry conditions, and restrained boundaries away from the toe of the slide; however, a more rigorous analysis could not be constrained realistically. 3D large-strain modelling, aimed at addressing the impact of block shapes and the interaction between blocks on failure kinematics (e.g.,

Bolla and Paronuzzi 2020), would require a detailed point cloud coverage of all block faces, which may not be achieved due to occlusions and the thick layer of debris filling the trench as well as the ground between B1 and B2. Monitoring demonstrates the role of rainfall in promoting instability of the frontal blocks, but water pressures are likely restricted to undefined preferential pathways within the slope. Understanding of the global structure and kinematics of the Quincinetto landslide, the existence of deep-seated shear zones, and the interplay between slow slope-scale movements and locally accelerated movements at the toe is similarly

Fig. 12 **a** Pairs of best-fitting planes derived from homologous clusters of points on the lateral and top sides of block B2. White points/planes/labels refer to the TLS-based survey (September 2019), yellow ones to the DLS-based survey (March 2022). **b** Detail of the downhill-facing lateral side of block B2, highlighting a relative shift of ~60 cm between the two point clouds. **c** Pair of best-fitting planes derived from a homologous cluster of points on the top side of block B5. White points/planes/labels refer to the TLS-based survey (September 2019), green ones to the DLS-based survey (March 2022). In (**a**) and (**c**), normal vectors to fitted planes have been flipped for better visualization in the case of overhanging rock surfaces (colour figure online)
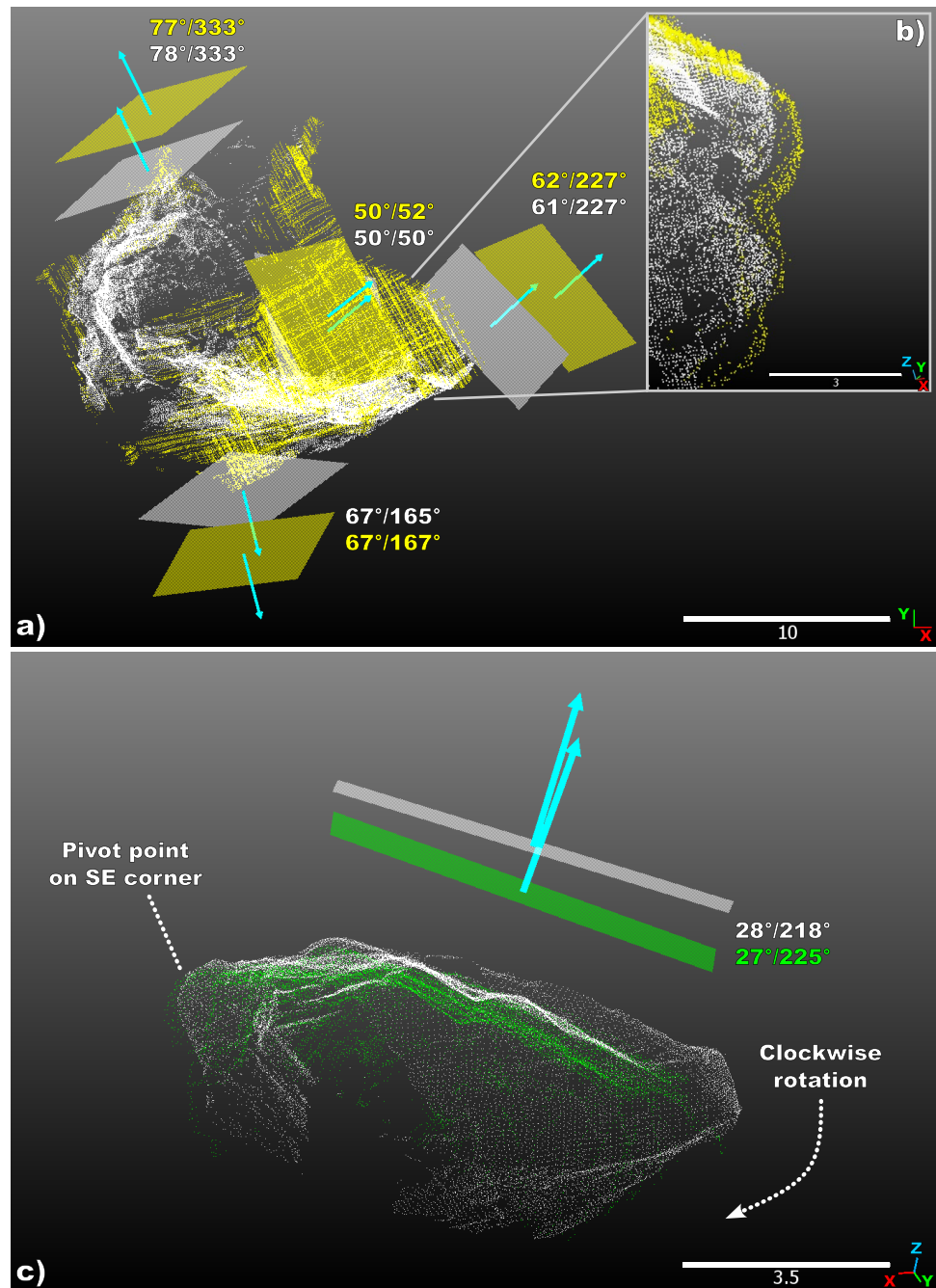
hindered by the impossibility to perform borehole drilling. In spite of the simplifications used, the obtained mechanical indicators appear in good agreement with acquired data and field evidences. This helps reduce interpretive uncertainties about the primary factors controlling instability of blocks B1/B2. More complex models may eventually be constrained by continued observation of the future evolution of the blocks.

Extensometer and GBInSAR measurements show higher activity at block B2 (Fig. 7a), with acceleration phases being triggered by rainfall and influenced by background velocity

(Fig. 10a). We interpret this rate-weakening behavior as a strong indication of basal slip along a through-going subplanar joint (scenario 1), where available shear strength is controlled by water pressures and the age of frictional contacts (Handwerger et al. 2016). As the latter decreases with renewed displacements (Dieterich 1979), the predisposition to instability in response to additional rainfall inputs temporarily increases. The markedly above-trend peak velocity of the December 2019 event, occurred when joint strength had just been reduced by a rapid sequence of major rainfall inputs (Fig. 7d), may on this basis be illustrative of

Table 2 Main sources of uncertainty in numerical analysis of the Quincinetto landslide

Source of model uncertainty	Description
Slope-scale kinematics	Lack of borehole cores and sub-surface monitoring prevents assessment of litho-structural changes with depth and identification of basal shear zones. Undefined relation between slow surface movements throughout the slide source area and locally accelerated movements at the toe. Sub-surface extent of the trench delimiting the frontal blocks and its relation with the sub-planar structure outcropping at the apex of the talus cone are also unknown
Rock mass properties	Access to in situ mica schist outcrops is possible only at the toe of the slope. Significant litho-structural heterogeneity (e.g., lens of impure marble in the headscarp area, large changes in degree of blockiness and disturbance of the mica schists). Simplified parametrization based on averaged RMR and assumed values of unit weight, Poisson's ratio, and tensile strength
Joint properties	Very high dispersion in orientation measurements. Simplified parametrization based on assumed values of residual friction angle and normal/shear stiffness
Brittle fracture damage	Undefined extent, geometry, and mechanical properties of brittle fracture damage features observed in parts of the frontal blocks. Representation by Voronoi tessellation may excessively amplify yielding in tension
Block shape	Rugged topography, dense vegetation, and thick deposits of chaotic debris prevent full 3D reconstruction of the larger blocks at the toe of the slide as well as possible identification of basal release surfaces
Water	No information on the location of preferential flow paths and the buildup of related water pressures during rainfall

conditions particularly close to runaway acceleration. Interestingly, a conspicuous flow of water was seen cascading down the talus cone for much of the period between late November and late December 2019. Further support to the attribution of the first modelling scenario to block B2 comes from the mainly translational shift of the TLS/DLS-surveyed block faces, the absence of block-scale tensile damage features, and the negligible rotations measured at tiltmeter T2. At the same time, we do not deem rotations measured at tiltmeter T3 to be representative of the global block kinematics, because the instrument is anchored to a rock exposure at the top of the S-facing lateral side that is fully enclosed by fine debris and weathered soil-like material (Fig. 5c). High kinematic freedom of this exposure would also explain the seemingly counterintuitive direction of rotation (i.e., towards B4/B5).

Acquired data motivate a slightly different assessment of block B1. This is characterized by rate-weakening behavior too, but displacements increased in response to a narrower group of rainfall events and, overall, are a fraction of those measured at block B2 (Figs. 7, 10). The rock mass exhibits well-developed tensile damage in connection with a 1 m wide sub-vertical fracture (Fig. 4e); with the other exception being the very top of the block, it appears poorly damaged elsewhere. In light of the above, we propose that scenarios 1 and 2 coexist to some extent in describing the underlying internal structure of B1. Concentrated tensile damage may originate from apparent cohesive strength of a basal slipping joint that, in comparison with B2, is subject to stronger dilation due to increased non-planarity and applied normal stress (Barton 2013). Since an infinite variation in geometry for a non-planar (undulating) rupture surface could be hypothesized, we incorporated an implicit basal cohesion term into scenario 1 by simulating a slightly discontinuous joint (i.e., with in-plane rock bridges) as determined by a continuity

factor of 0.8 and a unit length of sub-joints of 4 m. This leads to increased plastic strain and tensile yielding at the back of the block (see Fig. 13a for the "original" scenario 1 and Fig. 13b, c for the "modified" scenario 1), which is thus "split" in a sub-vertical manner by the induced differential movement. Two areas with distinct total displacements are in fact formed inside the block (Fig. 13d) consistently with the location of the aforementioned fracture intersecting B1, suggesting that its formation has been primarily conditioned by block kinematics. We observe that: (i) differential movement gradually reduces beginning from a tensile strength about three times higher (i.e., ~0.3 MPa) than what assumed here, which, however, may be less appropriate for the investigated rock mass; (ii) the spatial distribution of calculated strains and displacements is more significant than absolute values, as these are influenced by the convergence criteria of the shear strength reduction analysis, the model/mesh geometry, and the approximations to the connectivity of elements that must be satisfied in the solution procedure of the adopted code.

We rule out the presence of pervasive brittle fracture damage within B1 and B2 (scenario 3). Consistency in the dip of moving block faces (Fig. 12a, b), coupled with the abundance of rockfall boulders having volume in the order of 10^2–10^3 m^3 at the distal edge of the talus cone (Fig. 1a), validate the visual perception that brittle rock fracture affects proportionally small parts of the rock volumes, with limited effect on failure kinematics and potential rockfall magnitude. Scenario 3 may nevertheless represent the last evolutionary step before rapid detachment and fall, as stresses within the blocks are amplified by continued sliding towards steeper slopes. Reconstructing the past evolutionary steps of the blocks, in terms of the complex sequence of gravitational and glacial processes that led to their emplacement at the toe of the slide, is beyond the scope of the present work.
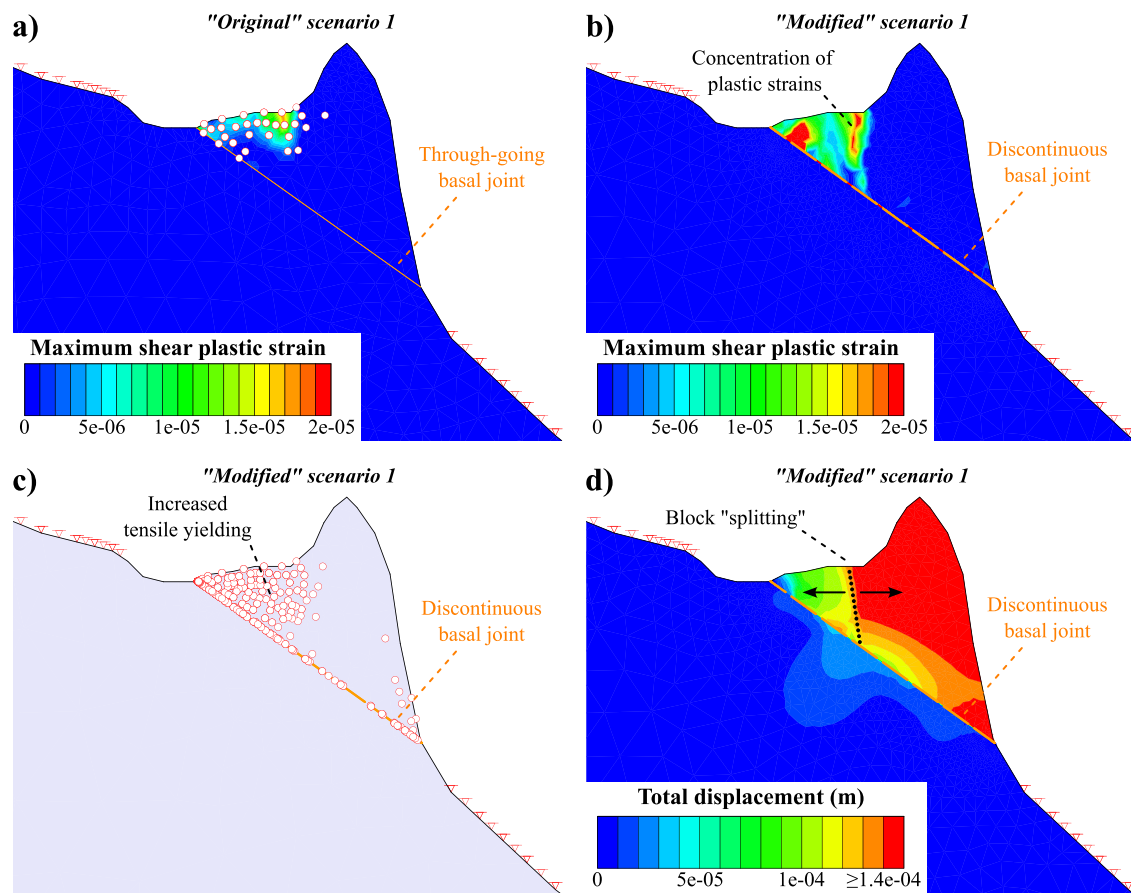
Fig. 13 Interpretation of the underlying internal structure of block B1. **a** Maximum shear plastic strains and tensile yielding induced by movement along a through-going basal joint (original scenario 1). **b, c** Respectively, concentration of maximum shear plastic strains and increased tensile yielding induced at the back of the block by movement along a slightly discontinuous basal joint (modified scenario 1) having the same in-plane trace of the through-going basal joint in (a). The two informative layers are reported in separate panels for better visualization. **d** Distribution of calculated total displacements. The black arrows are purely illustrative of the differential movement "splitting" the block; they are not scaled to movement direction or magnitude

6 Conclusions

The Quincinetto landslide exemplifies the potential challenges posed by large instabilities in steep alpine rock slopes. Prior failure to recognize its activity means that related hazards may not be currently avoided. Central to these hazards are two large discrete blocks at the toe of the slide having volume in excess of a thousand cubic meters. To obtain necessary information for the design of countermeasures, we constrained the kinematics of the blocks with respect to their underlying internal structure by integrating preliminary finite-element analysis, long-term displacement monitoring, and repeat laser scanning surveys.

In summary, we infer that ongoing block instability is promoted by an interplay of slow slope-scale deformation, local topography, and, significantly, transient degradation of friction on a through-going basal rupture surface of varying roughness, likely associated with an outcropping sub-planar structure inclined ~35° on the apex of the adjacent talus cone. Blocks B1 and B2 are also interpreted to translate as mostly individual entities with negligible influence of brittle fracture damage, though comprehensive 3D displacements could not be derived. Based on these findings and the dimensions of the blocks, stabilization by rock reinforcement may not be technically viable. A strategy could be to perform controlled blasting, limited in a first stage to the highly damaged—and more easily removable—upper parts of the blocks to examine the response in displacement activity through continued monitoring (providing that the highway can be protected from falling debris). Subsequent stages of blasting could be undertaken to resize the blocks and/or facilitate accessibility to the site, allowing the installation of additional instruments and thus enhancing monitoring.

We emphasize the importance of specifically tailoring rock slope investigations to the type of hazard at hand, the potential modes of failure, and the uncertainties to be

reduced, more so when accessibility to the site is exceedingly difficult. Advancements in numerical and technological tools now offer investigators the opportunity to more easily meet this task. On a related note, DLS-based surveying was here exploited for the explicit assessment of block kinematics. The acquired point cloud proved to be compatible in quality with its TLS-based counterpart, with the added benefit that much less effort was required to capture the three-dimensional (in places overhanging) geometry of blocks B1 and B2. While the orientation of moving block faces was tracked through plane-fitting of manually selected clusters of points, the unparalleled combination of high point cloud resolution and homogeneous point cloud density attainable by DLS devices over rugged topography opens the door to more streamlined procedures of change detection.

Further investigations may be devoted to the factors and mechanisms controlling deformation of the Quincinetto landslide at the overall scale, as well as the factors and mechanisms that controlled the initial collapse of the slope and the subsequent emplacement of the disaggregated slide mass. This would improve our understanding of the full range of present and future hazards, with special reference to the potential involvement of other large rock blocks in retrogressive instability at the toe of the slide.

Data Availability The data that support the findings of this study are available from the corresponding author upon reasonable request.

Declarations

Conflict of interest The authors have no competing interests to declare.

References

Agliardi F, Crosta GB, Meloni F, Valle C, Rivolta C (2013) Structurally-controlled instability, damage and slope failure in a porphyry rock mass. Tectonophysics 605:34–47

Atzeni C, Barla M, Pieraccini M, Antolini F (2015) Early warning monitoring of natural and engineered slopes with ground-based synthetic-aperture radar. Rock Mech Rock Eng 48:235–246

Barton N (2013) Shear strength criteria for rock, rock joints, rockfill and rock masses: problems and some solutions. J Rock Mech Geotech Eng 5:249–261

Barton N (1981) Shear strength investigations for surface mining. In: Proceedings of the 3rd international conference on stability in surface mining, Vancouver, Canada, 1–3 June, 1981, p 171–196

Beer G (1985) An isoparametric joint/interface element for finite element analysis. Int J Numer Methods Eng 21:585–600

Bieniawski ZT (1978) Determining rock mass deformability: experience from case histories. Int J Rock Mech Min Sci Geomech Abstr 15(5):237–247

Bieniawski ZT (1993) Classification of rock masses for engineering: the RMR system and future trends. In: Hudson JN (ed) Comprehensive rock engineering, vol 3. Elsevier, Pergamon, pp 553–573

Bolla A, Paronuzzi P (2020) Numerical investigation of the pre-collapse behavior and internal damage of an unstable rock slope. Rock Mech Rock Eng 53:2279–2300

Bordoni M, Bonì R, Colombo A, Lanteri L, Meisina C (2018) A methodology for ground motion area detection (GMA-D) using A-DInSAR time series in landslide investigation. CATENA 163:89–110

Brideau M-A, Pedrazzini A, Stead D, Froese C, Jaboyedoff M, van Zeyl D (2011) Three-dimensional slope stability analysis of South Peak, Crowsnest Pass, Alberta, Canada. Landslides 8:139–158

Brideau M-A, Sturzenegger M, Stead D, Jaboyedoff M, Lawrence M, Roberts N, Ward B, Millard T, Clague K (2012) Stability analysis of the 2007 Chehalis lake landslide based on long-range terrestrial photogrammetry and airborne LiDAR data. Landslides 9:75–91

Carlà T, Nolesini T, Solari L, Rivolta C, Dei Cas L, Casagli N (2019) Rockfall forecasting and risk management along a major transportation corridor in the Alps through ground-based radar interferometry. Landslides 16:1425–1435

Carlà T, Gigli G, Lombardi L, Nocentini M, Casagli N (2021) Monitoring and analysis of the exceptional displacements affecting debris at the top of a highly disaggregated rockslide. Eng Geol 294:106345

Casagli N, Catani F, Del Ventisette C, Luzi G (2010) Monitoring, prediction, and early warning using ground-based radar interferometry. Landslides 7:291–301

CloudCompare (2023) CloudCompare version 2.12.4 (computer program). 3D point cloud and mesh processing software. https://www.cloudcompare.org Accessed 4 Apr 2022

Crosta GB, Agliardi F, Rivolta C, Alberti S, Dei Cas L (2017) Long-term evolution and early warning strategies for complex rockslides by real-time monitoring. Landslides 14:1615–1632

Dieterich JH (1979) Modeling of rock friction: 1. Experimental results and constitutive equations. J Geophys Res Solid Earth 84(B5):2161–2168

Donati D, Stead D, Brideau M-A, Ghirotti M (2021) Using pre-failure and post-failure remote sensing data to constrain the three-dimensional numerical model of a large rock slope failure. Landslides 18:827–847

Eberhardt E (2008) Twenty-ninth Canadian Geotechnical Colloquium: the role of advanced numerical methods and geotechnical field measurements in understanding complex deep-seated rock slope failure mechanisms. Can Geotech J 45:484–510

Firpo G, Salvini R, Francioni M, Ranjith PG (2011) Use of digital terrestrial photogrammetry in rocky slope stability analysis by

distinct elements numerical methods. Int J Rock Mech Min Sci 48(7):1045–1054

Francioni M, Salvini R, Stead D, Litrico S (2014) A case study integrating remote sensing and distinct element analysis to quarry slope stability assessment in the Monte Altissimo area, Italy. Eng Geol 183:290–302

Francioni M, Salvini R, Stead D, Giovannini R, Ricucci S, Vanneschi C, Gullì D (2015) An integrated remote sensing-GIS approach for the analysis of an open pit in the Carrara marble district, Italy: slope stability assessment through kinematic and numerical methods. Comput Geotech 67:46–63

Francioni M, Salvini R, Stead D, Coggan J (2018) Improvements in the integration of remote sensing and rock slope modelling. Nat Haz 90:975–1004

Ghaboussi J, Wilson EL, Isenberg J (1973) Finite element for rock joints and interfaces. J Soil Mech Found Div 99(M10):833–848

Gianotti F, Forno MG, Ivy-Ochs S, Kubik PW (2008) New chronological and stratigraphical data on the Ivrea amphitheatre (Piedmont, NW Italy). Quat Int 190(1):123–125

Gigli G, Fanti R, Canuti P, Casagli N (2011) Integration of advanced monitoring and numerical modeling techniques for the complete risk scenario analysis of rockslides: the case of Mt. Beni (Florence, Italy). Eng Geol 120:48–59

Gischig V, Amann F, Moore JR, Loew S, Eisenbeiss H, Stempfhuber W (2011) Composite rock slope kinematics at the current Randa instability, Switzerland, based on remote sensing and numerical modeling. Eng Geol 118(1–2):37–53

Glastonbury J, Fell R (2010) Geotechnical characteristics of large rapid rock slides. Can Geotech J 47:116–132

Goodman RE, Taylor RL, Brekke TL (1968) A model for the mechanics of jointed rock. J Soil Mech Found Div 94(3):637–659

Gschwind S, Loew S, Wolter A (2019) Multi-stage structural and kinematic analysis of a retrogressive rock slope instability complex (Preonzo, Switzerland). Eng Geol 252:27–42

Hammah RE, Yacoub T, Corkum BC, Curran JH (2005) The shear strength reduction method for the generalized Hoek-Brown criterion. In: Proceedings of the 40th U.S. Rock Mechanics Symposium (USRMS), no. ARMA-05–810. Anchorage, Alaska, June 25–29, 2005

Hammah RE, Yacoub T, Corkum B, Curran JH (2008) The practical modelling of discontinuous rock masses with finite element analysis. In: Proceedings of the 42nd U.S. Rock Mechanics Symposium (USRMS), no. ARMA-08–180. San Francisco, California, June 29–July 2, 2008

Handwerger AL, Rempel AW, Skarbek RM, Roering JJ, Hilley GE (2016) Rate-weakening friction characterizes both slow sliding and catastrophic failure of landslides. Proc Natl Acad Sci USA 113(37):10281–10286

Havaej M, Coggan J, Stead D, Elmo D (2016) A combined remote sensing–numerical modelling approach to the stability analysis of Delabole Slate Quarry, Cornwall, UK. Rock Mech Rock Eng 49:1227–1245

Hoek E, Brown ET (1997) Practical estimates of rock mass strength. Int J Rock Mech Min Sci 34(8):1165–1186

Hoek E (2023). Practical rock engineering. https://www.rocscience.com/learning/hoeks-corner

ISRM (1978) Suggested methods for the quantitative description of discontinuities in rock masses. Int J Rock Mech Min Sci Geomech Abstr 15(6):319–368

Kenner R, Gischig V, Gojcic Z, Quéau Y, Kienholz C, Figi D, Thöny R, Bonanomi Y (2022) The potential of point clouds for the analysis of rock kinematics in large slope instabilities: examples from the Swiss Alps: Brinzauls, Pizzo Cengalo and Spitze Stei. Landslides 19:1357–1377

Leroueil S, Locat J, Vaunat J, Picarelli L, Lee H, Faure R (1996) Geotechnical characterization of slope movements. In: Proceedings of the 7th international symposium on landslides, vol. 1, pp. 53–74. Trondheim, Norway, 17–21 June 1996

Licata M, Fubelli G (2022) The GOGIRA system: an innovative method for landslides digital mapping. Geosciences 12(9):336

Luzi G, Pieraccini M, Mecatti D, Noferini L, Guidi G, Moia F, Atzeni C (2004) Ground-based radar interferometry for landslides monitoring: atmospheric and instrumental decorrelation sources on experimental data. IEEE Trans Geosci Remote Sens 42(11):2454–2466

Monserrat O, Crosetto M, Luzi G (2014) A review of ground-based SAR interferometry for deformation measurement. ISPRS J Photogramm Remote Sens 93:40–48

Paronuzzi P, Bolla A, Rigo E (2016) 3D stress-strain analysis of a failed limestone wedge influenced by an intact rock bridge. Rock Mech Rock Eng 49:3223–3242

Pieraccini M, Miccinesi L (2019) Ground-based radar interferometry: a bibliographic review. Remote Sens 11(9):1029

Rechberger C, Zangerl C (2022) Rock mass characterisation and distinct element modelling of a deep-seated rock slide influenced by glacier retreat. Eng Geol 300:106584

Riva F, Agliardi F, Amitrano D, Crosta GB (2018) Damage-based time-dependent modeling of paraglacial to postglacial progressive failure of large rock slopes. J Geophys Res Earth Surf 123(1):124–141

Rocscience (2023) RS2 version 11.018 (computer program). 2D geotechnical finite element analysis. https://www.rocscience.com/support/program-downloads Accessed 4 Apr 2022

Rossi G, Tanteri L, Tofani V, Vannocci P, Moretti S, Casagli N (2018) Multitemporal UAV surveys for landslide mapping and characterization. Landslides 15:1045–1052

SAV (2014) Opere di protezione dell'autostrada A5 nel tratto interessato dal fenomeno franoso in Comune di Quincinetto (TO), località Chiappetti. Unpublished technical report (in Italian)

Serra E, Valla PG, Gribenski N, Carcaillet J, Deline P (2022) Post-LGM glacial and geomorphic evolution of the Dora Baltea valley (western Italian Alps). Quat Sci Rev 282:107446

Spreafico MC, Francioni M, Cervi F, Stead D, Bitelli G, Ghirotti M, Girelli VA, Lucente CC, Tini MA, Borgatti L (2016) Back analysis of the 2014 San Leo landslide using combined terrestrial laser scanning and 3D distinct element modelling. Rock Mech Rock Eng 49:2235–2251

Spreafico MC, Sternai P, Agliardi F (2021) Paraglacial rock-slope deformations: sudden or delayed response? insights from an integrated numerical modelling approach. Landslides 18:1311–1326

Stead D, Coggan J (2012) Numerical modeling of rock-slope instability. In: Clague JJ, Stead D (eds) Landslides: types, mechanisms and modeling. Cambridge University Press, pp 144–158

Stead D, Jaboyedoff M, Coggan JS (2012) Rock slope characterization and geomechanical modelling. In: Eberhardt E, Froese C, Leroueil S, Turner K (eds) Landslides and engineered slopes: protecting society through improved understanding, vol 1. CRC Press, Boca Raton, pp 83–100

Strouth A, Eberhardt E (2009) Integrated back and forward analysis of rock slope stability and rockslide runout at Afternoon Creek, Washington. Can Geotech J 46:1116–1132

Sturzenegger M, Stead D (2012) The Palliser rockslide, Canadian Rocky Mountains: characterization and modeling of a stepped failure surface. Geomorphology 138:145–161

Wasowski J, Bovenga F (2014) Investigating landslides and unstable slopes with satellite Multi Temporal Interferometry: current issues and future perspectives. Eng Geol 174:103–138

Woods A, Hendry MT, Macciotta R, Stewart T, Marsh J (2020) GB-InSAR monitoring of vegetated and snow-covered slopes in remote mountainous environments. Landslides 17:1713–1726